POLITECNICO DI TORINO
Repository ISTITUZIONALE

Imidazole-imidazolate pair as organo-electrocatalyst for CO2 reduction on ZIF-8 material

(Article begins on next page)

02 January 2026

Imidazole-Imidazolate Pair as Organo-Electrocatalyst for CO₂ Reduction on ZIF-8 Material

Daniele Sassone**[a,b]*, *Sergio Bocchini[a]*, *Marco Fontana[a]*, *Clara Salvini[a,b]*, *Giancarlo Cicero***[b]*, *Michele Re Fiorentin[a]*, *Francesca Risplendi[b]*, *Giulio Latini[a]*, *M. Amin Farkhondehfal[a]*, *Fabrizio Pirri[a,b]*, *Juqin Zeng[a]*.

[a] Center for Sustainable Future Technologies (CSFT)@Polito, Istituto Italiano di Tecnologia, Via Livorno 60, 10144 Torino, Italy
[b] Department of Applied Science and Technology - DISAT, Politecnico di Torino, Corso Duca degli Abruzzi 24, 10129 Torino, Italy.

AUTHOR INFORMATION

Corresponding Authors

Daniele Sassone   daniele.sassone@iit.it   ORCID: 0000-0003-4343-4565
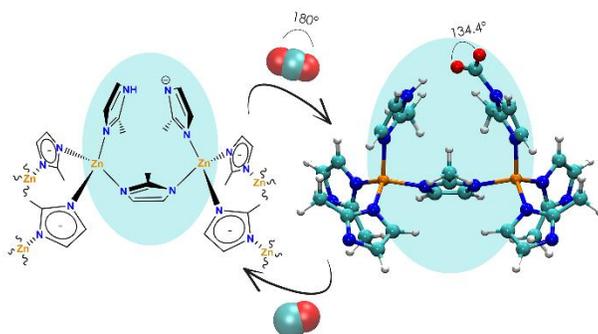Giancarlo Cicero   giancarlo.cicero@polito.it   ORCID: 0000-0002-2920-9882

Authors

Sergio Bocchini   sergio.bocchini@iit.it   ORCID: 0000-0003-2876-2317
Marco Fontana   marco.fontana@iit.it   ORCID: 0000-0003-0894-2193
Clara Salvini   clara.salvini@polito.it   ORCID: 0000-0002-8451-7896
Michele R. Fiorentin   michele.refiorentin@iit.it   ORCID: 0000-0002-1074-0411
Francesca Risplendi   francesca.risplendi@polito.it   ORCID: 0000-0002-1277-6733
Giulio Latini   giulio.latini@iit.it   ORCID: 0000-0003-3193-1898
Amin Farkhondehfal   amin.farkhondehfal@iit.it   ORCID: 0000-0002-5433-5653
Candido Fabrizio Pirri   fabrizio.pirri@polito.it   ORCID: 0000-0003-4991-9459
Juqin Zeng   juqin.zeng@iit.it   ORCID: 0000-0001-8885-020X

ABSTRACT: *The electrochemical reduction of CO₂ to value-added products is hindered by its thermodynamic stability and by the large energy required to chemically activate the molecule. With this respect, forcing CO₂ in a non-linear geometry would induce an internal electron charge rearrangement which would facilitate further electrochemical transformations. In this work, we achieved this goal through the design of a dual function electro-organocatalyst, which exploits the ability of the imidazolate (Im⁻) lone pair to bind CO₂ via nucleophilic attack and then*

electrochemically reduce it. To give structural stability to the Im⁻ based catalyst, the imidazoles species are incorporated into a solid structure, namely ZIF-8. Once activated by the organic Im⁻ ligand, CO₂ is electrochemically reduced to CO when a bias is applied to ZIF-8. The catalyst proposed in our study was first devised by computer aided design based on Density functional Theory simulations and then realized in laboratory. Our results demonstrate that ZIF-8 supported on conductive CNTs presents surface Im⁻ active sites which convert CO₂ into CO with a high faradaic efficiency (70.4%) at -1.2 V vs reversible hydrogen electrode, by combining chemical activation with electrochemical catalysis.

INTRODUCTION:

Through several types of catalysis, impeded reactions become accessible by lowering the required activation energy. Chemical, electrochemical and enzymatic catalysis are ubiquitous in the literature, however systems showing their cooperation are quite unusual. Combining chemical and electrochemical catalysis can be a suitable tool able to stand above the difficulties of several catalysis. ~~There are several examples of electroorganocatalysis reported in the literature in which they are classified as direct or indirect electrolysis depending on the possible presence of a redox mediator. The most known use of electro-organocatalysis comes from the organic synthesis, in which the active species is electrochemically generated (by an oxidation/reduction step) and then react with the substrate[1],[2],[3],[4]. A similar approach can also be found in the CO2 reduction reaction (CO2RR) by homogeneous catalysts. In these systems, the catalyst is a metal-organic complex, which is firstly reduced to form the nucleophilic active species and then reacts with CO2 starting the catalytic cycle. In this scenario, the metal-organic complex is a redox mediator, being firstly reduced and then reacting with the substrate, thus classifying the reaction as an electro metalorganocatalysis. Both in the homogeneous and heterogeneous catalysis of CO2RR, the metal centers are commonly considered the active sites, indeed for the latter, different examples of metalorganic complexes are able to convert CO2 into CO. The more consolidated compounds in literature are the bio-inspired porphyrins[5–7] (Fe, Co, Ni), the bipyridine metal complexes (Re, Mn)[8,9], which suffer from inevitably critical stability, complexes bearing pincer ligand (Ir, Mn)[10],[11],[12] and more sophisticated complexes having a double copper metal center coordinating pyridinic ligands[13],[14].~~ Examples of *electro-organocatalysis* are known in organic chemistry [1],[2],[3],[4] and also in the CO₂ reduction reaction (CO₂RR) performed by homogeneous

catalysts, in which the metal-organic complex is firstly reduced and then reacts with CO_2 starting the catalytic cycle. The metal centers are commonly considered the active sites of the CO_2RR, indeed the more consolidated homogeneous catalysts in literature are all metal organic complexes bearing several type of ligands: the bio-inspired porphyrins[5–7] (Fe, Co, Ni), the bipyridine (Re, Mn)[8,9], different pincer ligand (Ir, Mn)[10],[11],[12] and more sophisticated pyridinic ligands able to coordinate multi metallic sites[13],[14]. On the other hand, the heterogeneous catalysts for CO_2RR follow a similar pattern, in which the benchmark catalysts are based on metallic species and their relative oxides[15]. A proper electro-organocatalysis investigation for the CO_2RR, i.e. without the presence of active metal center, is instead a difficult proof to locate. Göttle and Koper were the first researchers to identify a reaction mechanism on porphyrin complexes, which do not involve the metal center as active species[16]. A possible catalysis conducted by mere organic molecules would be of extreme interest, since it could drastically reduce the cost of the catalyst, avoiding the employment of limited and often critical resources like the metals[17]. The synergic cooperation between the electrocatalysis facing an organocatalyst is a strategy that could open new routes for the electrochemical conversion of CO_2, currently dominated by expensive metallic compounds[18]. In a similar way in which the asymmetrical catalysis moved from metal-organic catalysis to a molecular one, as underlined by the recent Nobel prizes awarded to List and MacMillan[19],[20],[21], hopefully this work will inspire more interest into the design and the investigation on the activation of CO_2 by organic molecules.

The nucleophilicity of the imidazolate (Im^-), which reacts spontaneously with CO_2 causing a bending of the latter, is of extreme interest for the possible chemical activation of CO_2, since it reminds the radical anion $CO_2^{·-}$ obtained electrochemically at high investment of energy[22],[23]. In this work, through Density Functional Theory (DFT) modelling, a reaction to activate the CO_2 favoring its bending was studied. Combined with subsequent electrochemical steps for the CO_2 reduction and release, such system would represent an example of *electro-organocatalysis* for CO_2RR. A periodic structure like the one of the Zeolitic Imidazole Framework (ZIF) resulted to be a great preliminary candidate in order to display and organize imidazolate ligands able to perform the catalysis in heterogeneous conditions, thus avoiding all the limitations of a dissolved catalyst. ZIF-8 materials are well known in gas capture and separation application while only a few publications can be found for their use as catalyst for the CO_2RR[24],[25],[26],[27]. Nevertheless, the identification of the active sites on ZIF-8 materials is still far from completion. Indeed, at the date of this paper, to the best of our knowledge, only two previous works proposed a reaction mechanism supported by modelling. Both the investigations probed the aromatic sp^2 carbon sites present on the imidazolate ligand as possible catalytic centers, completely omitting the nitrogen sites[28],[29]. The formation of a C-C bond between the imidazole and the CO_2 molecule characterizes the proposed pathways, thus involving the aromaticity loss on the ligand[29]. This is an extremely energetic step, as underlined in the 2 eV step calculated in the work by Jiang et. al [28], which is even above the thermodynamic value of the one electron reduction of CO_2 known to be the highest possible energetic step for the reduction of this molecule[30]. Moreover, Dou et. al used a simplified clusters as the modelling structure, thus reducing the actual complexity of the

system[29]. All the same, these works proposed a mechanism involving critically uphill energy activation and neglected the spontaneous step involving the N$^-$ site present on the imidazolate ring.

In this work, a reaction mechanism was proposed taking in consideration the peculiar surface organization of ZIF-8 in which the co-presence of imidazole-imidazolate pairs resulted to be the main active species for the CO_2 activation. Further inorganic sites were investigated due to the presence of partial residual undercoordinated Zn sites able to perform the CO_2RR. The theoretical modelling also helped in the engineering of the ZIF-8 with the incorporation of multi-walled carbon nanotubes (MWCNTs). Indeed, the presence of a conductive support significantly reduced the activation energy of the electron transfer and experimentally aided the particle size reduction of the composite material. This strategy elucidated the tremendous advantages of chemical activation of CO_2 by simple organic molecules paired with the electrochemical reduction of it.

RESULTS AND DISCUSSION:

Simulated ZIF-8 structures and CO₂RR pathway

Ab initio Density Functional Theory (DFT) calculations were employed to investigate the selectivity for CO_2 reduction reaction at imidazole-based catalysts. Recent studies have proven that CO_2 can bind to imidazolate species[31],[32] by forming a Lewis acid-base adduct in which the CO_2 molecule is bent. Here we exploit such finding and prove that the activated CO_2 molecules can be further reduced via electrocatalytic transformation. A ZIF-8 material was chosen as model for the simulation of an ordered and robust imidazole-based structure in which Zn^{2+} cations have the role of anchoring the imidazolate anions[33] in an ordered crystalline arrangement that could be eventually deposited on a conductive electrode material. In particular, we focused on the low-index ZIF-8 (110) facets because of their larger stability[34],[35] and their prevalence in rhombic dodecahedron crystals, as those experimentally observed in the literature[36],[37],[38],[39]. Specifically, since CO_2 reduction reaction experiments are usually performed in slightly acidic conditions, we considered imidazole/imidazolate-terminated ZIF-8 (110) surfaces which recent computational investigations proved the thermodynamical stability of this surface termination in such pH range[40]. In this configuration the ZIF-8 (110) surfaces expose imidazole (*L-H) - imidazolate (*L) pairs (here the * indicate the underlying ZIF-8 structure) as represented in Figure 1a. The *L-H and *L species coordinate Zn^{2+} species which are 6.02 Å apart. This configuration is stabilized by a hydrogen bond (HB) established between the hydrogen atom of the *L-H and a nitrogen atom of the nearby *L.

Since ZIF-8 is not a good electric conductor, we also simulated its CO_2RR reactivity when deposited on a conductive nanostructure, i.e. a carbon nanotube. This system would be representative of a composite material able to perform both the chemical and electrochemical catalysis. The choice of a carbon based material avoids the utilization of precious inorganic materials and at the same time, introduces a more hydrophobic environment on the catalyst which

promotes the CO_2 reduction[41] and guarantees a stronger adherence of the catalyst on the electrode during the electrolysis. The effect of the carbon nanotubes was modelled by interfacing two ZIF-8 clusters of different sizes (ZC1@CNT and ZC2@CNT) with a metallic (8x8) carbon nanotube (Figure 1b and 1c). Smaller ZIF-8 clusters (ZC2@CNT) appear to be relevant to investigate size effects on the electrocatalytic performances.
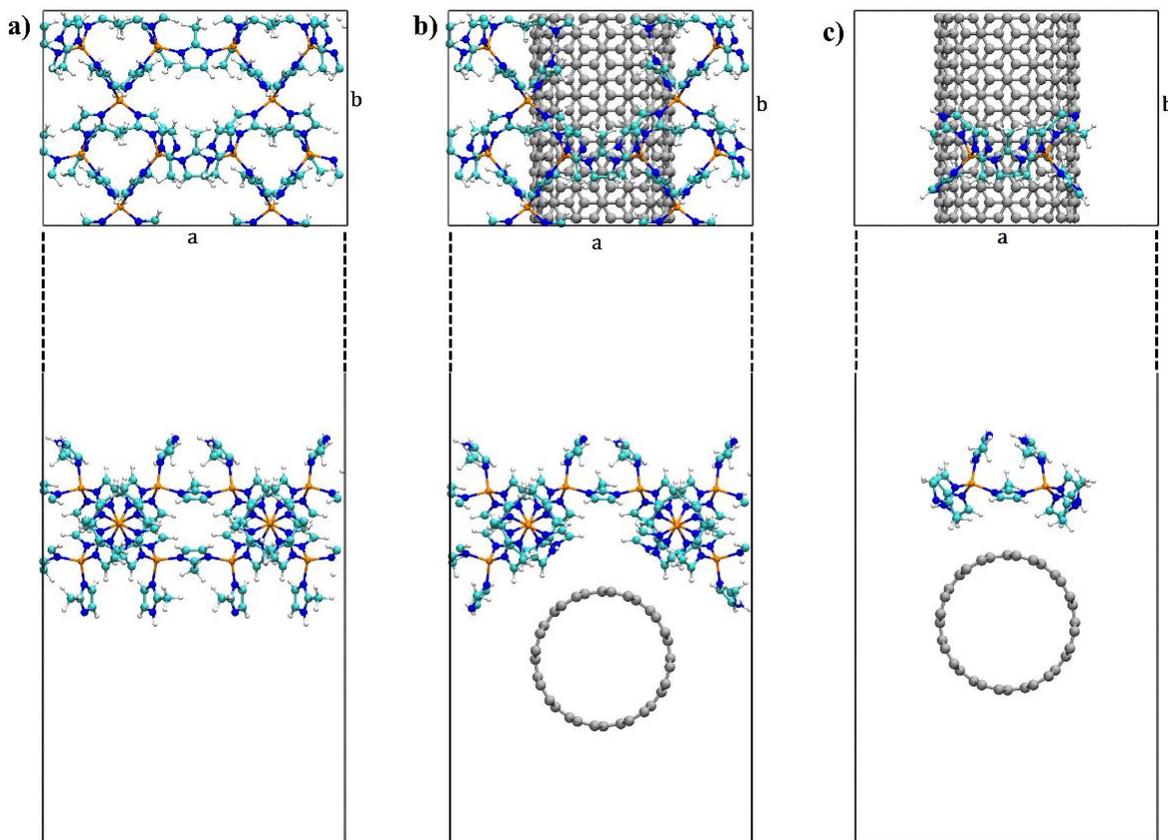

Figure 1: Ball-and-stick representations of simulated ZIF-8 structures: a) ZIF-8 (110) surface, b) ZC1@CNT and, c) ZC2@CNT. Atom color code: orange for zinc, blue for nitrogen, white for hydrogen, cyan and dark gray for carbon atoms in the ZIF structures, and CNT, respectively.

Since the stable ZIF-8 surface at operative reduction conditions exposes the *L-H/*L termination, and knowing that CO_2 can covalently bind to imidazolate species, we suggest and study the following CO_2RR mechanism:

$$CO_2 + 2H^+ + 2e^- \rightarrow CO + H_2O$$

Which unfolds into three steps,

$$*L\cdots H\text{-}L* + CO_2 \rightarrow *L\text{-}COO\cdots H\text{-}L* \qquad (1)$$

5

$$*\text{L-COO}\cdots\text{H-L*} + (\text{H}^+ + \text{e}^-) \rightarrow *\text{L-COOH}\cdots\text{H-L*} \tag{2}$$

$$*\text{L-COOH}\cdots\text{H-L*} + (\text{H}^+ + \text{e}^-) \rightarrow *\text{L}\cdots\text{H-L*} + \text{CO} + \text{H}_2\text{O} \tag{3}$$

yielding CO and H_2O. In the first step (1) a Lewis adduct *L-COO is formed in which the imidazolate nitrogen atom acts as Lewis base while the CO_2 as Lewis acid. Then two electrochemical reduction proton-electron coupled steps (2 and 3) occur, which lead to the release of the final products (CO and H_2O) and consequent regeneration of the active surface. Such pathway presents an analogous mechanism of a previous study, in which the CO_2RR reduction is completely performed without using the CO_2 dissolved in the electrolyte, or directly in the gas phase, rather in the form of carbamate bonded to the monoethanolamine [42].
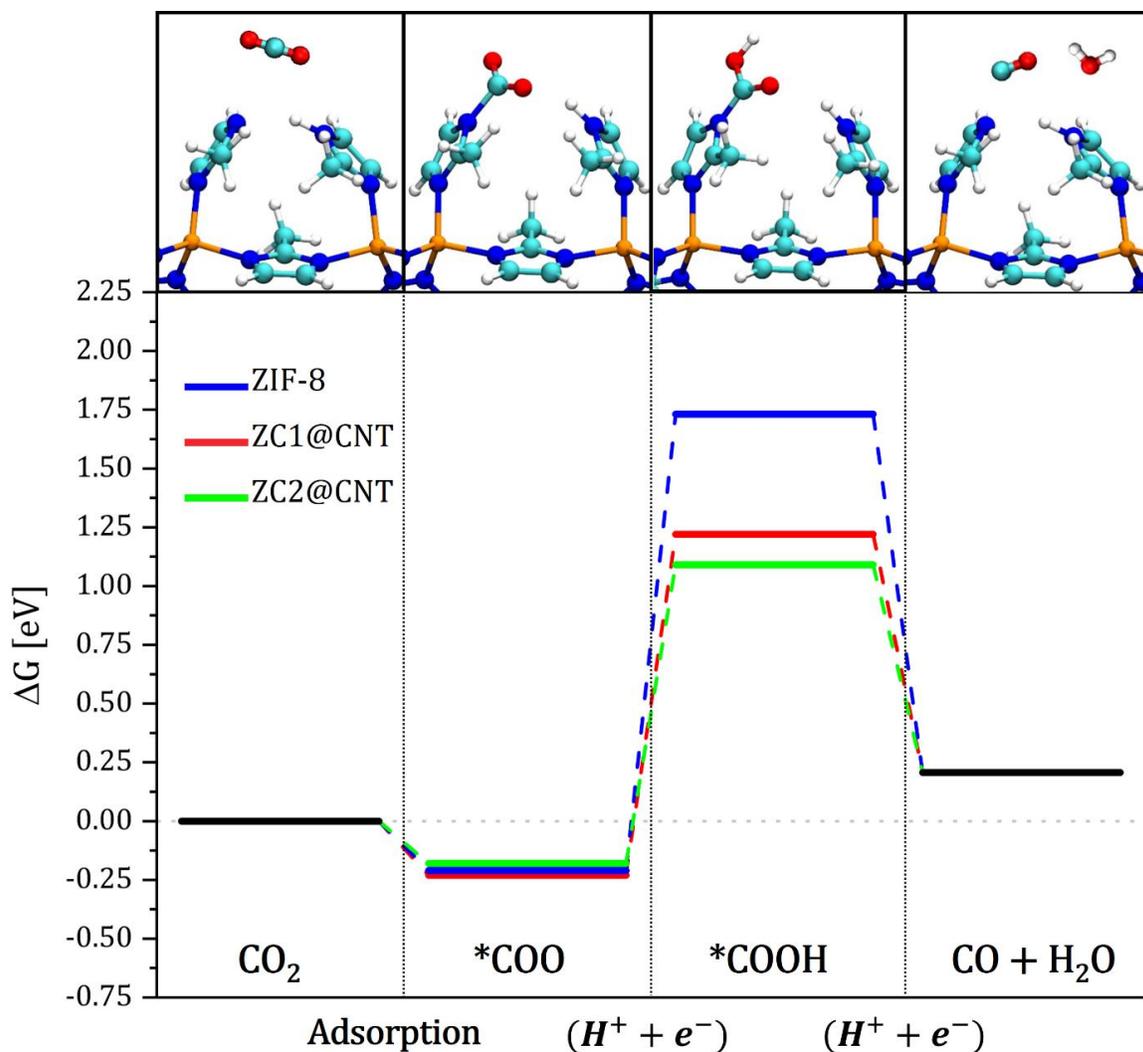
Figure 2: CO₂RR pathway forming CO and H₂O on ZIF-8 (blue line), ZC1@CNT (red line) and ZC2@CNT (green line) at U = 0 V vs RHE (lower panel). Ball-and-stick representation of reaction states (upper panel). Atom color code: orange for zinc, blue for nitrogen, white for hydrogen, red for oxygen and cyan for carbon.

Figure 2 shows the calculated free energy profile of the CO_2 electrochemical reduction reaction to CO and H_2O at U = 0 V vs RHE. The blue path corresponds to CO_2RR on ZIF-8 (110) surface (named ZIF-8), while the red and green lines represent the reduction steps on ZC1@CNT and ZC2@CNT, respectively. In all pathways, the first reaction step, i.e. the binding of the CO_2 to the *L site, is spontaneous ($\Delta G_{*CO2 \to *COO} < 0$). Upon the formation of *L-COO adduct, a C-N bond 1.569 Å long is formed. Consequently, the CO_2 molecule is bent (OCO angle of 134.39° degrees) and activated for subsequent reduction. This configuration is further stabilized by an HB between the *L-COO group and the nearby H-L* ligand. Such results evidence the great advantage of the CO_2 chemical activation compared to the high-energy electrochemical step. Moreover, it underlines the energetic benefits of the chemical interaction with the N⁻ site of the Im, rather than an electrochemical step which would involve the aromaticity loss[29],[28]. For all three pathways,

7

we found a similar energy trend which highlights that the overall reaction is not spontaneous at U = 0 V and a negative onset potential (U_{onset}^r) must be applied. The first electrochemical reduction step ($\Delta G_{*COO \rightarrow *COOH}$) is uphill and it determines the U_{onset}^r of the reaction for all considered model structures. The energy needed to convert *COO to *COOH is markedly higher on the ZIF-8 surface ($\Delta G_{*COO \rightarrow *COOH}$ = 1.95 eV) compared to that on the CNT supported ZIF-8 system ($\Delta G_{*COO \rightarrow *COOH}$ = 1.45 eV for ZC1@CNT). The presence of a metallic CNT support appears to facilitate the first proton-electron transfer to the *COO intermediate and decreases the $|U_{onset}^r|$ of about 0.5 eV. A further $|U_{onset}^r|$ decrease is observed by reducing the ZIF-8 cluster size in contact with the CNT (ZC2@CNT). Indeed, in the reaction path of the latter system U_{onset}^r is decreased to 1.27 eV, suggesting that a smaller ZIF-8 structure, and thus a closer proximity of the active site to the CNT surface, further improves the efficiency of the overall catalytic performances of the ZIF-8/CNT system. Such modelling investigation highlights an innovative clarification of the reaction pathway on ZIF-8 material unpublished before.

Despite the more stable surface exposing undercoordinated imidazole ligands, it is possible that in aqueous environment and at experimental conditions the ZIF-8 surfaces present defective Zn sites bonding to OH$^-$/H$_2$O species and not to Im$^-$/Im ligands[35]. For this reason we also studied how the reactivity of a ZIF-8 facet changes when the surface exposes zinc centers saturated with OH$^-$/H$_2$O (see supporting info Figure S.2). It is found that these sites are selective for HCOO$^-$ production. Since such surface metal coordination does not represent the most thermodynamically stable phase and it would rather represent minority surface defects, the production of HCOO$^-$ is expected to occur with low faradaic efficiency.

In summary, from a theoretical point of view, it is anticipated that ZIF-8 based electrocatalysts would present two possible kinds of active sites, the main molecular one originating from the Im and Im$^-$ pair selective for CO production and a secondary one, in which Im and Im$^-$ have been substituted by OH$^-$/H$_2$O, selective for HCOO$^-$.

Catalyst synthesis and characterizations

The modelled materials including a ZIF-8 framework (denoted as *sZIF-8)* and ZIF-8 grown on MWCNTs (denoted as s*ZIF-8-MWCNT*) were synthesized by using a new procedure in water solution. For the *ZIF-8* synthesis, 1.1 g of 2-methylimidazole (MIm, 13.4 mmol) and 591 mg of sodium hydroxide (NaOH, 14.8 mmol) were dissolved in 30 mL of bidistilled water. In other separated 30 mL of bidistilled water, 500 mg of [Zn(NO$_3$)$_2$·6H$_2$O] (1.68 mmol, Zn:MIm ratio 1:8) were dissolved. The latter solution was then added dropwise to the former under continuous sonication, which was kept cold by placing ice cubes in the sonication bath. Immediately after the first drop, the limpid basic solution turned into a white colloidal suspension. Once the two solutions were completely mixed, the sonication was kept for five minutes longer. The powder was separated by centrifugation and then washed twice with water and a third time with ethanol to remove the

excess of MIm and hydroxide. The final sample was eventually collected and dried under vacuum until constant weight was reached. Small aliquots of solvent were employed for the purification since the high level of dispersion of ZIF-8 in polar solvent. *sZIF-8-MWCNT* was prepared using a similar procedure but adding MWCNTs (50mg, 5% w/w) in the former basic solution and sonicating for at least 30 minutes before the addition of the latter salt solution. Sonication was performed in a cold bath which prevents the agglomeration of MWCNTs. The colloidal formation after the first drops was not clearly visible in this case due to the dark color of MWCNTs, while the precipitation of MWCNTs together with ZIF was visible in the middle of the process. In addition, a sample of bare MWCNTs was sonicated in the basic media, washed and dried for comparison. The same concentrations of NaOH and 2-methylimidazole were present in the solution for the treatment of MWCNTs in order to obtain the most similar conditions with those for the sZIF-8-MWCNT synthesis. Only the Zn salt was excluded with the aim of avoiding any contamination, because the Zn species in many other forms such as metal and metal oxide are reported to be active for the CO_2RR[43].

A morphological investigation was performed on both materials with Field Emission Scanning Electron Microscopy (FE-SEM) revealing large differences between *sZIF-8* and *sZIF-8-MWCNT* samples. Indeed, *sZIF-8* shows the typical rhombic dodecahedron morphology of micrometrical particles[36],[37],[38],[39] (Figure 3a). The incorporation of MWCNTs leads to drastic changes in both the size and morphology of the particles (Figure 3b). During the precipitation and agglomeration of ZIF-8, the MWCNTs were incorporated in the matrix. The dimension of the particles gets lower reaching the nanoscale dimension and the typical rhombic dodecahedron shape is totally lost, eventually causing the material amorphization. Such experiment data guided the modelling of the ZC2@CNT in which the cluster dimension is reduced.
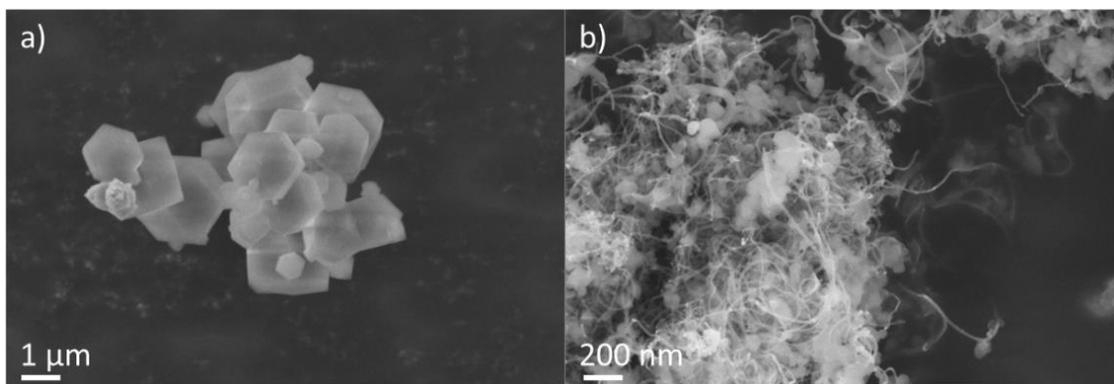

Figure 3: Electron microscopic images. a) FE-SEM images of sZIF-8 and b) sZIF-8-MWCNT.

The ATR spectra (Figure 4a) show a similar pattern for both materials demonstrating the formation of ZIF in presence of MWCNT. The peaks at 3130 and 2923 cm^{-1} are due to the C-H stretching of the aromatic carbons, the signals at 1669 cm^{-1} and 1590 cm^{-1} are respectively the C=C and C=N stretching modes of the imidazole. The three peaks at 1456, 1415 and 1306 cm^{-1} are the

stretching of the entire ring and the 1146 cm^{-1} is the C-N stretching mode. The 993 and 749 cm^{-1} can be assigned to the C-N and C-H bending modes. The 693 cm^{-1} is the ring-out-plane of the imidazole and the final 645 cm^{-1} of the interaction between Zn^{2+} cations with imidazolates, confirming the correct formation of the framework[44]. The ATR investigation additionally underlines the absence of signals at 3393 cm^{-1} and 3218 cm^{-1}. This is translated in the absence of Zn^{2+} cations involved in inorganic forms like ZnO and Zn(OH)$_2$ within the range of sensibility of the technique[45].

As shown in Figure 4b, X-Ray Diffraction (XRD) patterns were recorded and compared with the VESTA simulated diffraction pattern of a centered cubic structure having a $\overline{4}3m$ simmetry[46] and with the experimental ones from different publications[47],[48],[49]. For *sZIF-8* (green line), the diffraction peaks correspond to the ZIF-8 crystals planes of both simulated (red line) and the ones reported in the literatures, indicating the successful synthesis of highly crystalline ZIF-8. On the contrary, *sZIF-8-MWCNT* (blue line) shows a different pattern in which the well-defined peaks are partially covered by two broad bands at 13.97° and 26.13° with a minor contribution at around 45°. The bands with a maximum at 26.13° and 45°, respectively, are clearly associable with the main bands of MWCNT subject to the same treatment without zinc salt (Figure S.3), while the band with a maximum at 13.97° is the typical band reported in literature for amorphized ZIF-8[50],[51],[52]. Nevertheless, minor crystalline peaks are still present, meaning that the prepared ZIF-8 is not completely amorphous but rather a mixture of crystalline and amorphous regions. The drastic decrease in crystallinity is clearly due to the presence of nanotubes and a presumable π-π interaction of carbon nanotubes with the imidazoles which inhibit the crystal growth during the synthesis[53]. Due to nature of the application, the loss of the crystallinity and the consequent porous area is not a criticality like it could be in gas separation/sequestration technology, but rather an improvement for the electrocatalysis, since more defective sites bearing undercoordinated Im$^-$ site are exposed.

As a consequence of the amorphization, the materials also differ for their porosity (Figure S4, S5 and Table S2). sZIF-8 shows a high BET surface area and a large pore volume mainly attributed to micropores, which is typical of well-structured ZIF-8[27]. sZIF-8-MWCNT displays a relatively lower BET surface area and pore volume, to which meso- and macropores are the major contributors, confirming the significant influence of MWCNTs incorporation on the ZIF growth. The thermal decomposition was investigated by means of thermo-gravimetric analysis (TGA) coupled with gas phase infrared evolved gas analysis (EGA) to determine the degradation products (Figure S.6 and S.7). The two samples show similar degradations. Two main steps are present, the less crystalline structure of the composite material is confirmed by the less defined degradation steps *sZIF-8.* The presence of MWCNTs instead does not involve any significant effect on thermal stability. TGA analysis further guarantee the absence of inorganic species of zinc which would mutate the degradation pathway.

X-ray Photoelectron Spectroscopy (XPS) investigation provides several information about the chemical composition of the ligand and of the zinc center for *sZIF-8* (Figure S.8) and *sZIF-8-MWCNT* catalysts. All the values reported were calibrated with the C1s adventitious carbon placing it at 284.8 eV binding energy. In Figure 4c and 4d, the *sZIF-8-MWCNT* high-resolution spectra of N1s and C1s are reported. The nitrogen signal is deconvoluted in two main contributions: the C=N-C (399.1 eV) coming from the degenerate N^- of the imidazolate ligand Im^- and the C-NH-C (400.2 eV) of undercoordinated imidazole Im which restores the amino group[54]. Such value evidences the defects on the crystals as undercoordinated imidazoles, which support the mechanism involving the imidazole-imidazolate pair. In Figure 4d, the C 1s spectrum fitting is reported. Several contributions are present due to the imidazole ligand, C-C (285.6 eV), C-N (286.4 eV) and π-π^* (292.2 eV), but also due to adventitious carbon, C adv. (284.8 eV), and its oxidized form, C-O-C (287.9 eV). In the region of Zn 2p (Figure S.9), the typical doublet of Zn is recorded. The $2p_{3/2}$ signal requires two functions to be deconvoluted, the main Zn-N (1022.5 eV)[55] from the Zn coordinating the imidazolate ligand and a generic Zn-OH (1021.6 eV) coming from undercoordinated Zn^{2+} sites which reacts to water in order to balance the charge[45,56]. The water is actually coordinated as H_2O molecule and OH^- ligands in order to balance the stoichiometry charge of the surface in presence of under-coordination. O 1s region (Figure S.9) shows a small contribution derived from the water coordinated H_2O/OH^-, namely OH-Zn (531.5 eV)[45] and also from part of the oxidized adventitious carbon O-C (532.8 eV). It is important to underline the impossibility from Zn signals to discriminate between ZnO and $Zn(OH)_2$ species, since both peaks would fall in the same binding energy regions. A different case is the one of the O signal, in which these peaks are perfectly separated and help us to discriminate the absence of ZnO nanoparticles in our catalyst[57].
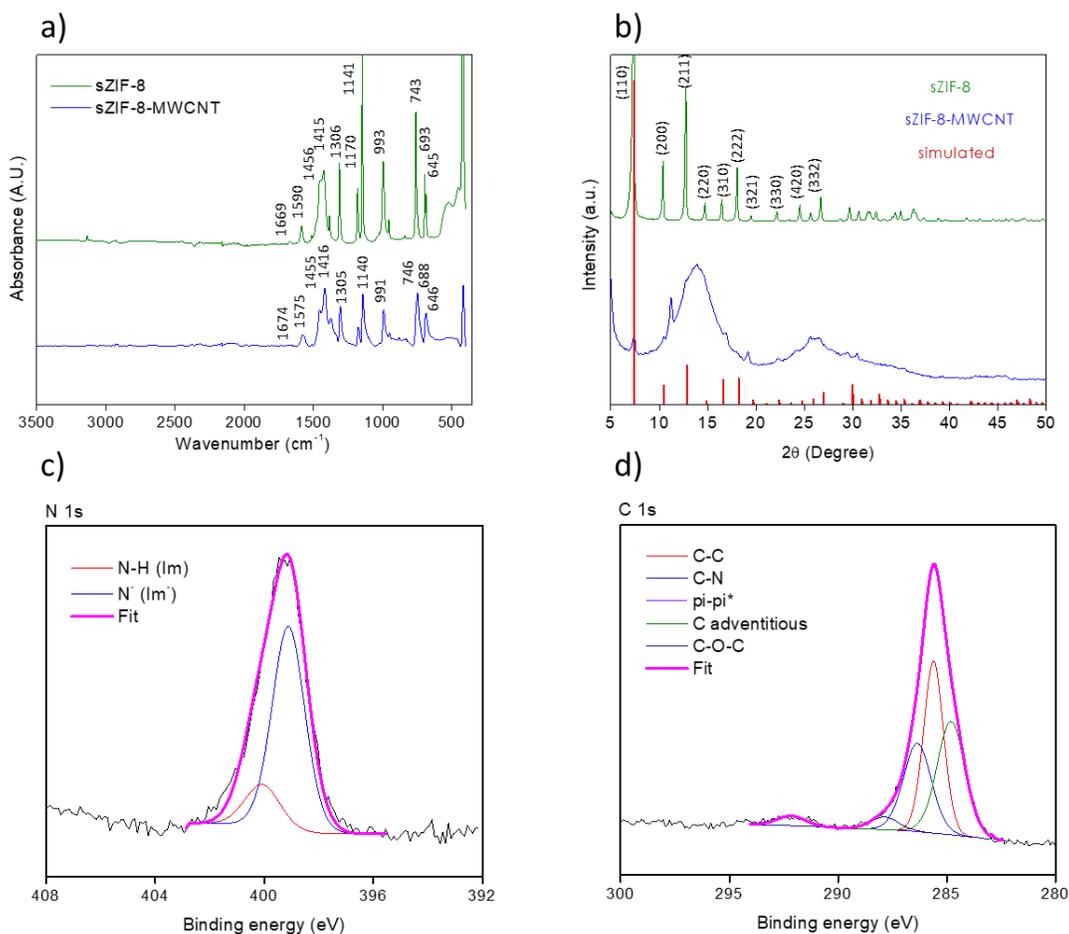
Figure 4: a) ATR spectrum of sZIF-8 (green) and sZIF-8-MWCNT (blue) sample. b) XRD patterns of sZIF-8 (green), sZIF-8-MWCNT (blue), ZIF-8 simulated (red). XPS spectra of sZIF-8-MWCNT of c) N_{1s} and d) C_{1s} regions.

From the previous analyses, it can be concluded that the MWCNT incorporation affects the growth of ZIF-8 particles, as evidenced by the remarkable changes in morphology, crystallinity and porosity, but the hybrid material indeed preserves the coordination geometry of ZIF-8, as observed by various spectroscopic analyses.

Chronoamperometric tests were performed to realize the CO_2 electrolysis with modelled catalyst. The reported potentials refer to the RHE hereafter. The *sZIF-8* and *sZIF-8-MWCNT* electrodes were tested in a 0.1 M $KHCO_3$ solution with a batch cell configuration (Figure S.10a), showing the best selectivity of 48.7% and 65.7%, respectively for the CO_2RR (FE_{CO2RR}) at -1.2 V. In addition to a lower FE for the former, a low current density of 5.7 mA cm^{-2} and poor stability was also found. Such low current density is due to the intrinsic low electrical conductivity of ZIF-8[58] and the stability is correlated to its strong interaction with the polar electrolyte. *sZIF-8* catalyst detaches from the gas diffusion layer (GDL) substrate during the electrolysis leading to the support exposure to the electrolyte, which inevitably favors the hydrogen production[59]. Such problem does not occur with the *sZIF-8-MWCNT*, which results firmly attached to the electrode and shows a higher current density of 7.0 mA cm^{-2} in the same batch cell setup. MWCNT

introduces hydrophobicity to the material, which prevent its detachment from the electrode. Finally, also the treated MWCNT were investigated showing a strictly selectivity toward the competitive HER. The three catalysts performances, analyzed in batch cell setup and 0.1 M $KHCO_3$ electrolyte, are reported in the SI in the Figure S.13.

Once the better experimental performances of the *sZIF-8-MWCNT* had been established, this catalyst was further tested in a semi-flow cell configuration (Figure S.10b) with different concentrations of $KHCO_3$ water solution (0.1, 0.5, 1.0 and 2.0 M) and at different potentials (-1.2, -1.0 and -0.8 V). The use of a semi-flow cell setup aimed at increasing the mass diffusion rates at larger current densities (> 10 mA cm^{-2}) and enabling the long-term stability tests. Stable i-t curves are observed in all the tests. Complete information about relative selectivity and current densities are reported in Figure S.11 and Table S.3 in the SI. In general, the current density increases with increasing the $KHCO_3$ concentration at each potential (Figure 5a), the same for the FE_{H2} and FE_{HCOO^-} except for the value in 0.5 M, where lower hydrogen evolution was registered. Indeed, the highest selectivity for carbon monoxide is reached in 0.5 M $KHCO_3$, registered a FE_{CO} of 65.8% and an overall FE_{CO2RR} of 70.4% at -1.2 V (Figure 5a). However, despite the great selectivity, this electrolyte leads to a lower current density (Figure 5a, red line) compared to the more concentrated ones. Taking into account the overall electrode activity at the same potential, the 1.0 M $KHCO_3$ results in the highest turnover frequency number (TOF_{CO2RR}) value of 230.4 h^{-1} (Figure 5b) considering the number of N atoms forming the active site. With respect to the secondary products HCOO$^-$, it is clearly visible that in Figure 5a the FE_{HCOO^-} grows parallel to the $KHCO_3$ concentration in the electrolyte. Since formate production is correlated to the presence of surface Zn site coordinated to OH^-/H_2O species, Figure S.1 and S.2, it is plausible that in an electrolyte having a higher dielectric constant, i.e. more salt dissolved, the dissociation of the coordinated water molecules can be easier with a better shielding of zinc charge. Such results are of great interest compared to the actual literature. Indeed, the great hydrophobicity introduced by the MWCNT makes it possible the catalyst evaluation on the flow cell setup, which guarantees great performances in terms of reachable current density (**Errore. L'origine riferimento non è stata trovata.**). ZIF-8 catalysts are often tested only inside H-cell reactor, probably due to their

instability in operando conditions, quite often the actual duration of the electrolysis and the relatively stability is a missing data.

Table 1: State of the art for the ZIF-8 based catalysts.

Catalyst	Electrolyte	Potential (V vs RHE)	Current density (mA cm^{-2})	FE_{CO2RR} (%)	Cell setup	Time (h)	Ref.
ZIF-8	0.25 M K_2SO_4	-1.2 V	~11 mA cm^{-2}	~80%	H-type	n.r.	[28]
ZIF-8	0.1 M $KHCO_3$	-1.2 V	n.r.	<50%	H-type	n.r.	[29]
ZIF-A-LD-CB	0.1 M $KHCO_3$	-1.0 V	~3 mA cm^{-2}	>80%	H-type	10 h	[29]
Sn-ZIF-8	0.5 M $KHCO_3$	-1.1 V	27 mA cm^{-2}	>74 %	H-type	1 h	[49]
ZIF-8$_{SO4}$	0.5 M NaCl	-1.2 V	~3.5 mA cm^{-2}	65.5 %	H-type	n.r.	[24]
ZIF-8$_{NO3}$	0.5 M NaCl	-1.2 V	~2 mA cm^{-2}	69.8 %	H-type	n.r.	[24]
ZIF-8$_{Ac}$	0.5 M NaCl	-1.2 V	~1 mA cm^{-2}	57.7 %	H-type	n.r.	[24]
ZIF-8-MWCNT	0.5 M $KHCO_3$	-1.2 V	13.4 mA cm^{-2}	70.4 %	Flow cell	16 h	This work
ZIF-8-MWCNT	1.0 M $KHCO_3$	-1.2 V	42.7 mA cm^{-2}	70.6 %	Flow cell	40 h	This work

To evaluate the best conditions of stability and operability several prolonged electrolysis tests were performed on the sZIF-8-MWCNT catalyst. A 20-hour test at -1.2 V vs RHE in 0.1 M $KHCO_3$ shows a good retention of selectivity along all the hours, in terms of selectivity, current density (Figure 5c) and CO production rate (Figure 5d) with a value over the 0.05 mmol h^{-1}cm^{-2} at -1.2 V in 0.1 M $KHCO_3$. A stability test of more than 40 hours in 1.0 M $KHCO_3$ electrolyte was also performed (Figure S.12). After the highest value of 0.13 mmol h^{-1} cm^{-2} registered in the first

few hours, a quite stable value of 0.8 mmol h^{-1} cm^{-2} was obtained in the remaining time, showing only a minor rise with time due to the accumulation of formate in recirculating electrolyte.
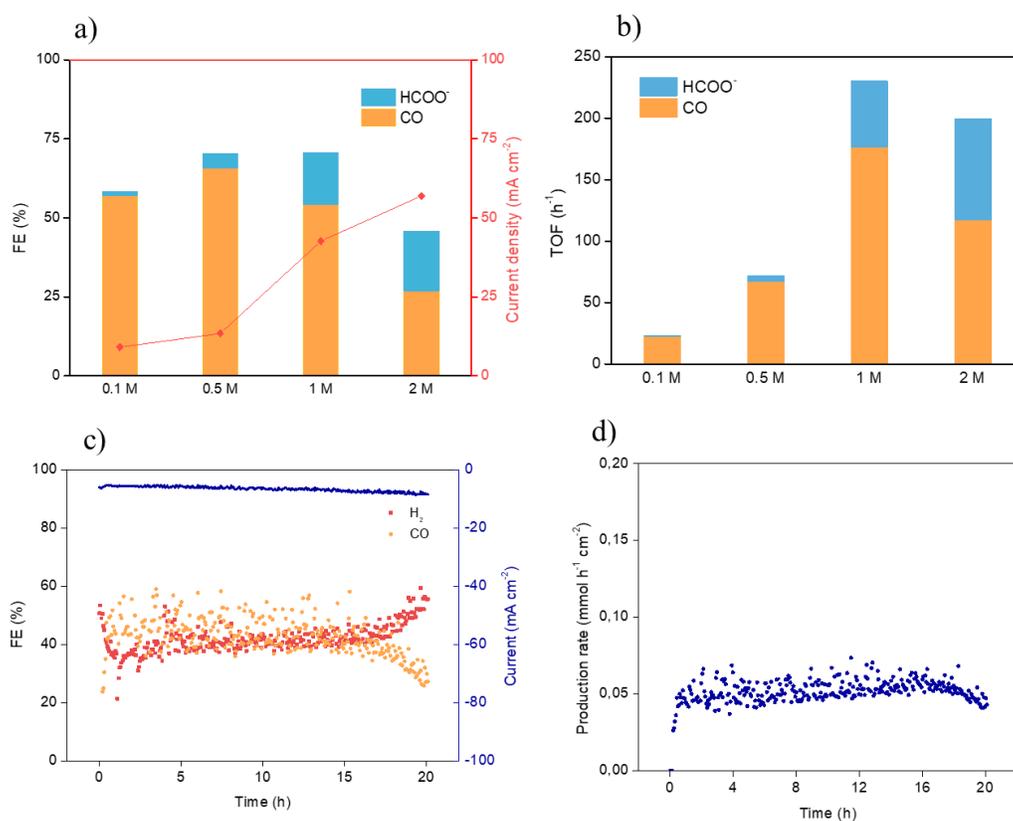

Figure 5: semi-flow cell CO$_2$RR investigation on sZIF-8-MWCNT electrodes. a) FEs and current densities at -1.2 V in different electrolyte compositions and b) the relative TOFs. Stability test in 0.1 M KHCO$_3$ at -1.2 V vs RHE c) FE and current density as a function of time and d) CO production rate during a 20-hour stability test.

As a counterproof of the role of the imidazole supported on ZIF-8 catalyst, an electrode composed only by treated MWCNTs was tested at the same conditions and showed no selectivity for the CO$_2$RR, producing only H$_2$. Hence, it is possible to state that ZIF-8 and MWCNTs play synergic roles in the CO$_2$RR, in which the former provides selective and active imidazole-imidazolate sites able to perform the catalytic and electrocatalytic reduction of CO$_2$, while the MWCNT favors the electrical conductivity of the catalyst increasing also the overall stability.

CONCLUSION:

In conclusion, an ~~innovative strategy~~ interesting method for guiding the synthesis of a heterogeneous catalyst by theoretical modelling was ~~proposed~~ exposed. With the aim of overcoming the difficulties of the electrochemical activation of CO$_2$, a combined chemical-electrochemical reduction process was investigated. DFT modelling reveals a ~~interesting~~ CO$_2$RR mechanism on an imidazole-based framework, in which the CO$_2$ is chemically activated by the

imidazole bending the linear structure of the substrate, and two subsequent electrochemical steps allow further reduction to CO_2. Furthermore, CNT incorporation is predicted to enhance the electron transport in the catalyst. Experimental data demonstrate that both ZIF-8 and ZIF-8-MWCNT show interesting selectivity for the CO_2RR to CO and the performance of the latter is enhanced, perfectly matching the theoretical prediction. The herein proposed theory-guided catalyst design not only provides new opportunities for the industrialization of CO_2 conversion, but also opens novel visions for synthesis of new catalysts which merge together the organocatalysis with the electrochemical one. Further studies will be performed in order to realize new strategies to support pure imidazoles molecules as active catalysts, without their incorporation inside metal organic framework, in order to reach a complete electro-organo catalysis for the CO_2RR.

EXPERIMENTAL METHOD:

Density Functional Theory calculations (DFT):

The theoretical predictions are based on Density-Functional Theory (DFT) carried out with the Quantum Espresso package[60][61]. All the calculations are performed with the Perdew-Burke-Ernzerhof (PBE) functional[62] and the Kohn–Sham equations are solved using ultrasoft pseudopotentials[63] to describe the electron-ion interaction. Periodic boundary conditions are imposed and the Brillouin zone was sampled at the Γ point. For all calculations, a plane-wave energy cutoff of 28 Ry (280 Ry) for the wave functions (electron densities) was adopted. The convergence of forces and energy was set to 10^{-4} Ry and 10^{-5} Ry/Bohr, respectively.

The optimized ZIF-8 bulk was obtained by a full relaxation of both cell parameters and atom positions. To simulate the (110) facet, a 2D slab was built introducing a vacuum layer of 20 Å along the direction perpendicular to the surface to avoid undesired interactions between periodic replicas. We used a metallic (8x8) carbon nanotube (CNT) to simulate the experimental MWCNTs.

To study the performances of the proposed electrocatalysts towards the CO_2RR the Gibbs free energy (G) profiles of the pathway leading to CO were computed within the Computational Hydrogen Electrode (CHE) method proposed by Nørskov and collaborators[64][65]. Because of the systematic errors in the total energies of CO and CO_2 introduced by the PBE functional, statistical corrections to OCO-molecules (reactants, intermediates, and products)[66] were computed. Finally, solvation energies were estimated as reported in the supporting information (Section 1 and Table S1 of SI).

Materials and synthesis: zinc nitrate hexahydrated ([$Zn(NO_3)_2 \cdot 6H_2O$], 297.49 gmol^{-1} 98%), 2-methylimidazole (Mim, 82.11 gmol^{-1} 99%), sodium hydroxide (NaOH, 39,99 g mol^{-1} 98%), multiwalled carbon nanotube (MWCNT, 98%) and bidistilled water (MilliQ). *A*ll the chemicals were purchased from Merck without further purification.

X-Ray Diffraction (XRD): patterns were recorded in Bragg-Brentano symmetric geometry by using a PANalyti-cal X'Pert Pro instrument (Cu-Ka radiation, 40 kV and 30 mA) equipped with an X'Celerator detector.

Field-emission scanning electron microscopy (FESEM): the images were recorded on a ZEISS Supra 40 FESEM with the following configuration: SE2 detector for secondary-electron imaging, BSE detector for back-scattered electron imaging, Si(Li) Oxford Instruments detector for Energy-Dispersive X-ray (EDX) Spectroscopy.

Brunauer–Emmett–Teller surface analysis (BET): The specific surface area and the macro/micropore volume/area of the crystals were measured using a Micromeritics gas adsorption analyzer ASAP 2020 Plus 2.00 instrument equipped with commercial software for calculation and analysis. The BET surface area was calculated from the adsorption isotherms using the standard Brunauer–Emmett–Teller (BET) equation. The mesopore and micropore volume was obtained using a BJH plot.

Thermo-gravimetric and evolved gas analyses (TGA-EGA): TGA were carried out on a Netzsch TG 209 F1 Libra while EGA was conducted by means of a Bruker Tensor II infrared spectrophotometer equipped with vapor phase accessory and DTGS detector. The two instrument were coupled by a heated gas transfer line. About 10 mg of sample were placed in an alumina pan and heated up to 800°C in nitrogen flow (20 ml min^{-1}) followed by an 15 minutes long isotherm.

Attenuated Total Reflectance Fourier Transform Infrared spectroscopy (ATR-FT-IR): ATR analysis was performed on a Bruker Tensor II in transmission mode placing the pure sample on the surface of the crystal. The analysis was performed in the range of 4000-400 cm^{-1}.

X-ray photoelectron spectroscopy (XPS): the analysis was performed with a PHI 5000 Versaprobe spectrometer (Physical Electronics), equipped with monochromatic Al K-alpha X-ray source (1486.6 eV). Surface charge compensation was obtained with a combined system, based on an electron gun and Ar$^+$ ion gun. Survey and high resolution (HR) spectra were acquired using pass energy (PE) values of 187.85 and 23.50 eV, respectively. The calibration of the binding energy (BE) scale was obtained by setting the adventitious C component of the C1s region to 284.8 eV. Casa XPS software was used for the analysis of the experimental data. The Shirley background function was subtracted from HR spectra to remove the background signal[67]. The reported uncertainties on relative atomic concentrations were calculated with Monte Carlo routines implemented in Casa XPS.

Electrochemical Setup: the as-prepared catalysts were coated onto a carbon paper (GDL; SIGRACET 28BC, SGL Technologies) in order to enable the electrochemical evaluation of the powder-like materials towards the CO$_2$RR. 3 mg of catalyst (*sZIF-8* or *sZIF-8-MWCNT*) were dispersed in 160 μL of iPrOH by sonication. The obtained uniform slurry was then drop-casted on the GDL and dried in air overnight. Each electrode has a catalyst loading of 2 mg cm^{-2}.

Chronoamperometry (CA): tests were performed with a CHI 760D (CH Instruments, Inc.) potentiostat in a customized two-compartment cell (ElectroCell™) with a proton exchange membrane (Nafion Membrane N117, Ion Power). Both cathodic and anodic compartments are connected to a mechanical pump which promotes the circulation of electrolyte at 2 mL min^{-1}. A catalyst-coated carbon paper of 1.5 cm^2 was used as the working electrode, a Pt foil as the counter and a Ag/AgCl (1 mm, leak-free LF-1) as the reference. Gas-phase products were analyzed on-line by a micro gas chromatograph (µGC, Fusion®, INFICON) with two channels containing a 10m Rt-Molsieve 5A column and an 8 m Rt-Q-Bond column, respectively. Both channels are equipped with a micro thermal conductivity detector (micro-TCD). The inlet of the µGC equipment was connected to the cathodic side of the electrochemical cell through a GENIE filter to remove the humidity from the gas. During the CA measurements, a constant CO_2 flow rate of 25 ml min^{-1} was maintained back site to the electrode (gas-diffusion layer) to saturate the electrolyte and to bring the gaseous products to the µGC. Liquid products were analyzed by a High-Performance Liquid Chromatograph (Thermo Scientific Ultimate3000 HPLC) with a UV-Vis Detector set at 210 nm by using a ReproGel (300 × 8 mm) column, with 9.0 mM H_2SO_4 (flow rate of 1.0 mL min^{-1}) as mobile phase. The faradaic efficiency (FE) for each product was calculated by dividing the coulombs needed to produce the actual determined amount of this product by the total coulombs consumed during the corresponding reduction period of each measurement. Batch cell experiment was also conducted for *sZIF-8* with analogous configuration but absence of liquid pump and purging CO_2 flow inside the electrolyte both for cathodic and anodic compartments.

ASSOCIATED CONTENT

No potential competing interest was reported by the authors.

Supporting Information.

Major details about computational modelling, XRD, Isotermal linear plot, TGA and EGA, XPS, cell configuration, chronoamperometric tests, stability tests and are reported in the supporting information.

Zeng contributed to the work conceptualization. All authors contributed to the composition of the manuscript.

REFERENCES

[1]   Francke R, Little RD. Redox catalysis in organic electrosynthesis: Basic principles and recent developments. Chem Soc Rev 2014;43:2492–521. https://doi.org/10.1039/c3cs60464k.

[2]   Jensen KL, Franke PT, Nielsen LT, Daasbjerg K, Jørgensen KA. Anodic oxidation and organocatalysis: Direct regio- And stereo-selective access to meta-substituted anilines by α-arylation of aldehydes. Angew Chemie - Int Ed 2010;49:129–33. https://doi.org/10.1002/anie.200904754.

[3]   Schämann M, Schäfer HJ. Reaction of enamines and mediated anodic oxidation of carbohydrates with the 2,2,6,6-tetramethylpiperidine-1-oxoammonium ion (TEMPO+). Electrochim Acta 2005;50:4956–72. https://doi.org/10.1016/j.electacta.2005.02.077.

[4]   Zalewska K, Santos MM, Zalewska K, Santos MM, Cruz H, Branco LC, et al. chapter Electro- Organocatalysis Processes Organocatalysis Processes. Recent Adv Organocatalysis 2016.

[5]   Torbensen K, Joulié D, Ren S, Wang M, Salvatore D, Berlinguette CP, et al. Molecular Catalysts Boost the Rate of Electrolytic CO 2 Reduction . ACS Energy Lett 2020:1512–8. https://doi.org/10.1021/acsenergylett.0c00536.

[6]   Torbensen K, Han C, Boudy B, von Wolff N, Bertail C, Braun W, et al. Iron Porphyrin Allows Fast and Selective Electrocatalytic Conversion of CO2 to CO in a Flow Cell. Chem - A Eur J 2020;26:3034–8. https://doi.org/10.1002/chem.202000160.

[7]   Guo Z, Cheng S, Cometto C, Anxolabéhère-Mallart E, Ng S-M, Ko C-C, et al. Highly Efficient and Selective Photocatalytic CO 2 Reduction by Iron and Cobalt Quaterpyridine Complexes. J Am Chem Soc 2016;138:9413–6. https://doi.org/10.1021/jacs.6b06002.

[8]   Rotundo L, Garino C, Priola E, Sassone D, Rao H, Ma B, et al. Electrochemical and Photochemical Reduction of CO 2 Catalyzed by Re(I) Complexes Carrying Local Proton Sources. Organometallics 2018. https://doi.org/10.1021/acs.organomet.8b00588.

[9]   Franco F, Cometto C, Nencini L, Barolo C, Sordello F, Minero C, et al. Local Proton Source in Electrocatalytic CO2 Reduction with [Mn(bpy–R)(CO)3Br] Complexes. Chem - A Eur J 2017;23:4782–93. https://doi.org/10.1002/chem.201605546.

[10]   Bertini F, Glatz M, Stöger B, Peruzzini M, Veiros LF, Kirchner K, et al. Carbon Dioxide Reduction to Methanol Catalyzed by Mn(I) PNP Pincer Complexes under Mild Reaction Conditions. ACS Catal 2019;9:632–9. https://doi.org/10.1021/acscatal.8b04106.

[11]   Talukdar K, Issa A, Jurss JW. Synthesis of a redox-active NNP-type pincer ligand and its

application to electrocatalytic CO2 reduction with first-row transition metal complexes. Front Chem 2019;7:1–11. https://doi.org/10.3389/fchem.2019.00330.

[12]   Feller M, Gellrich U, Anaby A, Diskin-Posner Y, Milstein D. Reductive Cleavage of CO2 by Metal-Ligand-Cooperation Mediated by an Iridium Pincer Complex. J Am Chem Soc 2016;138:6445–54. https://doi.org/10.1021/jacs.6b00202.

[13]   Bouwman E, Angamuthu R, Byers P, Lutz M, Spek AL. Electrocatalytic CO2 Conversion to Oxalate by a Copper Complex. Science (80-) 2010;327:313–5. https://doi.org/10.1126/science.1177981.

[14]   Pokharel UR, Fronczek FR, Maverick AW. Reduction of carbon dioxide to oxalate by a binuclear copper complex. Nat Commun 2014;5:1–5. https://doi.org/10.1038/ncomms6883.

[15]   Wang Y, Liu J, Wang Y, Al-Enizi AM, Zheng G. Tuning of CO2 Reduction Selectivity on Metal Electrocatalysts. Small 2017;13:1–15. https://doi.org/10.1002/smll.201701809.

[16]   Göttle AJ, Koper MTM. Determinant Role of Electrogenerated Reactive Nucleophilic Species on Selectivity during Reduction of CO2 Catalyzed by Metalloporphyrins. J Am Chem Soc 2018;140:4826–34. https://doi.org/10.1021/jacs.7b11267.

[17]   European Commission. Study on the review of the list of Critical Raw Materials - Critical Raw Materials Factsheets. 2017. https://doi.org/10.2873/876644.

[18]   Henckens T. Critical raw materials. Gov World's Miner Resour 2021:61–70. https://doi.org/10.1016/b978-0-12-823886-8.00023-3.

[19]   Ahrendt KA, Borths CJ, Macmillan DWC, January R V. New Strategies for Organic Catalysis : The First Highly Enantioselective Organocatalytic Diels - Alder Reaction Over the past 30 years , enantioselective catalysis has become one of the most important frontiers in exploratory organic synthetic research . 2000:4243–4.

[20]   MacMillan DWC. The advent and development of organocatalysis. Nature 2008;455:304–8. https://doi.org/10.1038/nature07367.

[21]   List B, Lerner RA, Iii CFB, Torrey N, Road P, Jolla L, et al. Proline-Catalyzed Direct Asymmetric Aldol Reactions The Skaggs Institute for Chemical Biology and the Department of Molecular Biology The Scripps Research Institute Most enzymatic transformations have a synthetic counterpart . Often though , the mechanism 2000:2395–6.

[22]   Janik I, Tripathi GNR. The nature of the CO2- radical anion in water. J Chem Phys 2016;144. https://doi.org/10.1063/1.4946868.

[23]   Li W. Electrocatalytic Reduction of CO2 to Small Organic Molecule Fuels on Metal Catalysts 2010:27–43.

[24]   Wang Y, Hou P, Wang Z, Kang P. Zinc Imidazolate Metal–Organic Frameworks (ZIF-8) for Electrochemical Reduction of CO2 to CO. ChemPhysChem 2017;18:3142–7.

https://doi.org/10.1002/cphc.201700716.

[25] Guan W, Dai Y, Dong C, Yang X, Xi Y. Zeolite imidazolate framework (ZIF)-based mixed matrix membranes for CO2 separation: A review. J Appl Polym Sci 2020;137:1–13. https://doi.org/10.1002/app.48968.

[26] Babu DJ, He G, Hao J, Vahdat MT, Schouwink PA, Mensi M, et al. Restricting Lattice Flexibility in Polycrystalline Metal–Organic Framework Membranes for Carbon Capture. Adv Mater 2019;31:6–11. https://doi.org/10.1002/adma.201900855.

[27] Mu L, Liu B, Liu H, Yang Y, Sun C, Chen G. A novel method to improve the gas storage capacity of ZIF-8. J Mater Chem 2012;22:12246–52. https://doi.org/10.1039/c2jm31541f.

[28] Jiang X, Li H, Xiao J, Gao D, Si R, Yang F, et al. Carbon dioxide electroreduction over imidazolate ligands coordinated with Zn(II) center in ZIFs. Nano Energy 2018;52:345–50. https://doi.org/10.1016/j.nanoen.2018.07.047.

[29] Dou S, Song J, Xi S, Du Y, Wang J, Huang ZF, et al. Boosting Electrochemical CO2 Reduction on Metal–Organic Frameworks via Ligand Doping. Angew Chemie - Int Ed 2019;58:4041–5. https://doi.org/10.1002/anie.201814711.

[30] Matsubara Y, Grills DC, Kuwahara Y. Thermodynamic Aspects of Electrocatalytic CO2 Reduction in Acetonitrile and with an Ionic Liquid as Solvent or Electrolyte. ACS Catal 2015;5:6440–52. https://doi.org/10.1021/acscatal.5b00656.

[31] Izadyar M, Rezaeian M, Victorov A. Theoretical study on the absorption of carbon dioxide by DBU-based ionic liquids. Phys Chem Chem Phys 2020;22:20050–60. https://doi.org/10.1039/d0cp03612a.

[32] Zhu X, Song M, Xu Y. DBU-Based Protic Ionic Liquids for CO2 Capture. ACS Sustain Chem Eng 2017;5:8192–8. https://doi.org/10.1021/acssuschemeng.7b01839.

[33] Kaneti YV, Dutta S, Hossain MSA, Shiddiky MJA, Tung KL, Shieh FK, et al. Strategies for Improving the Functionality of Zeolitic Imidazolate Frameworks: Tailoring Nanoarchitectures for Functional Applications. Adv Mater 2017;29:1–31. https://doi.org/10.1002/adma.201700213.

[34] Pang SH, Han C, Sholl DS, Jones CW, Lively RP. Facet-specific stability of ZIF-8 in the presence of acid gases dissolved in aqueous solutions. Chem Mater 2016;28:6960–7. https://doi.org/10.1021/acs.chemmater.6b02643.

[35] Chizallet C, Bats N. External surface of zeolite imidazolate frameworks viewed ab initio: Multifunctionality at the organic-inorganic interface. J Phys Chem Lett 2010;1:349–53. https://doi.org/10.1021/jz900192x.

[36] Schejn A, Aboulaich A, Balan L, Falk V, Lalevée J, Medjahdi G, et al. Cu2+-doped zeolitic imidazolate frameworks (ZIF-8): Efficient and stable catalysts for cycloadditions and condensation reactions. Catal Sci Technol 2015;5:1829–39.
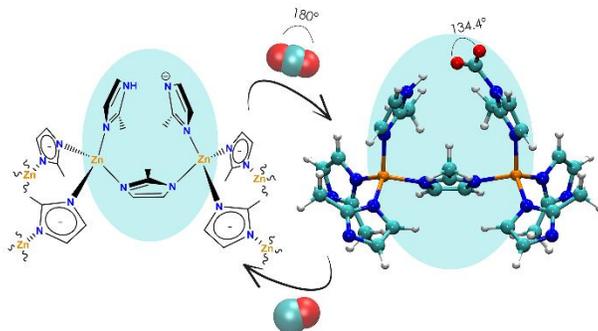
https://doi.org/10.1039/c4cy01505c.

[37]   Goyal S, Shaharun MS, Kait CF, Abdullah B, Ameen M. Photoreduction of carbon dioxide to methanol over copper based zeolitic imidazolate framework-8: A new generation photocatalyst. Catalysts 2018;8. https://doi.org/10.3390/catal8120581.

[38]   Pan Y, Liu Y, Zeng G, Zhao L, Lai Z. Rapid synthesis of zeolitic imidazolate framework-8 (ZIF-8) nanocrystals in an aqueous system. Chem Commun 2011;47:2071–3. https://doi.org/10.1039/c0cc05002d.

[39]   Cravillon J, Münzer S, Lohmeier SJ, Feldhoff A, Huber K, Wiebcke M. Rapid room-temperature synthesis and characterization of nanocrystals of a prototypical zeolitic imidazolate framework. Chem Mater 2009;21:1410–2. https://doi.org/10.1021/cm900166h.

[40]   Weng T, Schmidt JR. Structure and Thermodynamic Stability of Zeolitic Imidazolate Framework Surfaces. J Phys Chem C 2020;124:1458–68. https://doi.org/10.1021/acs.jpcc.9b10124.

[41]   Ott S, Orfanidi A, Schmies H, Anke B, Nong HN, Hübner J, et al. Ionomer distribution control in porous carbon-supported catalyst layers for high-power and low Pt-loaded proton exchange membrane fuel cells. Nat Mater 2020;19:77–85. https://doi.org/10.1038/s41563-019-0487-0.

[42]   Lee G, Li YC, Kim JY, Peng T, Nam DH, Sedighian Rasouli A, et al. Electrochemical upgrade of CO2 from amine capture solution. Nat Energy 2021;6:46–53. https://doi.org/10.1038/s41560-020-00735-z.

[43]   Lourenco MAO, Zeng J, Jagdale P, Castellino M, Sacco A, Farkhondehfal MA, et al. Biochar/Zinc Oxide Composites as Effective Catalysts for Electrochemical CO2Reduction. ACS Sustain Chem Eng 2021;9:5445–53. https://doi.org/10.1021/acssuschemeng.1c00837.

[44]   Zhang Y, Jia Y, Li M, Hou L. Influence of the 2-methylimidazole/zinc nitrate hexahydrate molar ratio on the synthesis of zeolitic imidazolate framework-8 crystals at room temperature. Sci Rep 2018;8:1–7. https://doi.org/10.1038/s41598-018-28015-7.

[45]   Winiarski J, Tylus W, Winiarska K, Szczygieł I, Szczygieł B. XPS and FT-IR Characterization of Selected Synthetic Corrosion Products of Zinc Expected in Neutral Environment Containing Chloride Ions. J Spectrosc 2018;2018. https://doi.org/10.1155/2018/2079278.

[46]   Momma K, Izumi F. VESTA 3 for three-dimensional visualization of crystal, volumetric and morphology data. J Appl Crystallogr 2011;44:1272–6. https://doi.org/10.1107/S0021889811038970.

[47]   Nordin NAHM, Ismail AF, Misdan N, Nazri NAM. Modified ZIF-8 mixed matrix membrane for CO2/CH4 separation. AIP Conf Proc 2017;1891. https://doi.org/10.1063/1.5005424.

[48] Liédana N, Galve A, Rubio C, Téllez C, Coronas J. CAF@ZIF-8: One-step encapsulation of caffeine in MOF. ACS Appl Mater Interfaces 2012;4:5016–21. https://doi.org/10.1021/am301365h.

[49] Geng W, Chen W, Li G, Dong X, Song Y, Wei W, et al. Induced CO_2 Electroreduction to Formic Acid on Metal−Organic Frameworks via Node Doping. ChemSusChem 2020;13:4035–40. https://doi.org/10.1002/cssc.202001310.

[50] Cao S, Bennett TD, Keen DA, Goodwin AL, Cheetham AK. Amorphization of the prototypical zeolitic imidazolate framework ZIF-8 by ball-milling. Chem Commun 2012;48:7805–7. https://doi.org/10.1039/c2cc33773h.

[51] Wu X, Yue H, Zhang Y, Gao X, Li X, Wang L, et al. Packaging and delivering enzymes by amorphous metal-organic frameworks. Nat Commun 2019;10:1–8. https://doi.org/10.1038/s41467-019-13153-x.

[52] Bennett TD, Cao S, Tan JC, Keen DA, Bithell EG, Beldon PJ, et al. Facile mechanosynthesis of amorphous zeolitic imidazolate frameworks. J Am Chem Soc 2011;133:14546–9. https://doi.org/10.1021/ja206082s.

[53] Hameed N, Church JS, Salim N V., Hanley TL, Amini A, Fox BL. Dispersing single-walled carbon nanotubes in ionic liquids: A quantitative analysis. RSC Adv 2013;3:20034–9. https://doi.org/10.1039/c3ra42488j.

[54] Mohtasebi A, Chowdhury T, Hsu LHH, Biesinger MC, Kruse P. Interfacial Charge Transfer between Phenyl-Capped Aniline Tetramer Films and Iron Oxide Surfaces. J Phys Chem C 2016;120:29248–63. https://doi.org/10.1021/acs.jpcc.6b09950.

[55] Tuncel D, Ökte AN. Improved Adsorption Capacity and Photoactivity of ZnO-ZIF-8 Nanocomposites. Catal Today 2021;361:191–7. https://doi.org/10.1016/j.cattod.2020.04.014.

[56] Tian F, Cerro AM, Mosier AM, Wayment-Steele HK, Shine RS, Park A, et al. Surface and stability characterization of a nanoporous ZIF-8 thin film. J Phys Chem C 2014;118:14449–56. https://doi.org/10.1021/jp5041053.

[57] Duchoslav J, Steinberger R, Arndt M, Stifter D. XPS study of zinc hydroxide as a potential corrosion product of zinc: Rapid X-ray induced conversion into zinc oxide. Corros Sci 2014;82:356–61. https://doi.org/10.1016/j.corsci.2014.01.037.

[58] Kim D, Kim DW, Hong WG, Coskun A. Graphene/ZIF-8 composites with tunable hierarchical porosity and electrical conductivity. J Mater Chem A 2016;4:7710–7. https://doi.org/10.1039/c6ta01899h.

[59] Zeng J, Fontana M, Sacco A, Sassone D, Pirri CF. A study of the effect of electrode composition on the electrochemical reduction of CO_2. Catal Today 2021. https://doi.org/10.1016/j.cattod.2021.07.014.

[60] Enkovaara J, Rostgaard C, Mortensen JJ. Advanced capabilities for materials modelling with Q uantum ESPRESSO n.d.

[61] Giannozzi P, Baroni S, Bonini N, Calandra M, Car R, Cavazzoni C, et al. QUANTUM ESPRESSO: A modular and open-source software project for quantum simulations of materials. J Phys Condens Matter 2009;21. https://doi.org/10.1088/0953-8984/21/39/395502.

[62] Perdew JP, Burke K, Ernzerhof M. Generalized gradient approximation made simple. Phys Rev Lett 1996;77:3865–8. https://doi.org/10.1103/PhysRevLett.77.3865.

[63] Smith JM, Jones SP, White LD. Soft self-consistent pseudopotentials in a generalized eigenvalue formalism. Gastroenterology 1977;72:193. https://doi.org/10.1016/S0016-5085(77)80340-5.

[64] Nørskov JK, Rossmeisl J, Logadottir A, Lindqvist L, Kitchin JR, Bligaard T, et al. Origin of the overpotential for oxygen reduction at a fuel-cell cathode. J Phys Chem B 2004;108:17886–92. https://doi.org/10.1021/jp047349j.

[65] Rossmeisl J, Qu ZW, Zhu H, Kroes GJ, Nørskov JK. Electrolysis of water on oxide surfaces. J Electroanal Chem 2007;607:83–9. https://doi.org/10.1016/j.jelechem.2006.11.008.

[66] Risplendi F, Re Fiorentin M, Cicero G. Unravelling electrocatalytic properties of metal porphyrin-like complexes hosted in graphene matrices. 2D Mater 2020;7. https://doi.org/10.1088/2053-1583/ab6a5f.

[67] Shirley DA. High-resolution x-ray photoemission spectrum of the valence bands of gold. Phys Rev B 1972;5:4709–14. https://doi.org/10.1103/PhysRevB.5.4709.

Imidazole-Imidazolate Pair as Organo-Electrocatalyst for CO$_2$ Reduction on ZIF-8 Material

Daniele Sassone*†‡, Sergio Bocchini†, Marco Fontana†, Clara Salvini†‡, Giancarlo Cicero*‡, Michele Re Fiorentin†, Francesca Risplendi‡, Giulio Latini†, M. Amin Farkhondehfal†, Fabrizio Pirri†‡, Juqin Zeng†.

ABSTRACT: *The electrochemical reduction of CO$_2$ to value-added products is hindered by its thermodynamic stability and by the large energy required to chemically activate the molecule. With this respect, forcing CO$_2$ in a non-linear geometry would induce an internal electron charge rearrangement which would facilitate further electrochemical transformations. In this work, we achieved this goal through the design of a dual function electro-organocatalyst, which exploits the ability of the imidazolate (Im$^-$) lone pair to bind CO$_2$ via nucleophilic attack and then electrochemically reduce it. To give structural stability to the Im$^-$ based catalyst, the imidazoles species are incorporated into a solid structure, namely ZIF-8. Once activated by the organic Im$^-$ ligand, CO$_2$ is electrochemically reduced to CO when a bias is applied to ZIF-8. The catalyst proposed in our study was first devised by computer aided design based on Density functional Theory simulations and then realized in laboratory. Our results demonstrate that ZIF-8 supported on conductive CNTs presents surface Im$^-$ active sites which convert CO$_2$ into CO with a high faradaic efficiency (70.4%) at -1.2 V vs reversible hydrogen electrode, by combining chemical activation with electrochemical catalysis.*